Dental Materials 42 (2026) 790–806

Contents lists available at ScienceDirect

Dental Materials

journal homepage: www.elsevier.com/locate/dental

Early-stage stability and degradation of patient-specific biodegradable 3D-printed implants for critical mandibular reconstruction

Hsuan-Wen Wang [a,b], Chiao-Min Chang [a,b], Yen Cheng [a], Egidijus Šimoliūnas [c], Pao-Wei Lee [a], Wei-Che Tsai [a], Chun-Li Lin [a,b,*]

[a] Department of Biomedical Engineering, National Yang Ming Chaio Tung University, Taipei, Taiwan
[b] Medical Device Innovation & Translation Center, National Yang Ming Chiao Tung University, Taipei, Taiwan
[c] Department of Biological Models, Institute of Biochemistry, Life Sciences Centre, Vilnius University, Lithuania

ARTICLE INFO

Keywords:
Biodegradable implant
Mandibular reconstruction
PCL/β-TCP composite
Topology optimization
Gradient lattice design
Finite element analysis
Hydrolytic degradation
Dynamic loading simulation

ABSTRACT

Objective: This study aimed to develop patient-specific biodegradable mandibular implants composed of polycaprolactone (PCL) reinforced with 30 wt% β-tricalcium phosphate (β-TCP) using fused deposition modeling (FDM), and to evaluate how gradient lattice structural designs influence early postoperative mechanical stability and degradation behavior in critical-sized mandibular defects, thereby establishing practical design criteria for reliable reconstruction.

Methods: Gradient lattice architectures were designed by finite element–based topology optimization, assigning dense lattices (P06, ~1000 μm pores) to high-stress regions and larger pores (P08, ~1500 μm) to low-stress zones. Two implant spans were investigated: RI-2, with an arc length approximately twice the average bone width, and RI-3, with an arc length about three times the bone width. Mechanical properties were characterized by tensile and four-point bending tests, and a dual-mode platform applied hydrolytic degradation and cyclic loading (20–200 N, 1 Hz) to replicate early postoperative oral conditions.

Results: The PCL/β-TCP composite showed an elastic modulus of 450 ± 20 MPa and cell viability of average 84.5 %. Four-point bending revealed that the RI-2 design achieved a proof load of 83.8 ± 5.3 N and bending strength of 1466 ± 92 N·mm, 2.35-fold higher than RI-3. Under dual hydrolysis–loading, all RI-2 implants maintained structural integrity for one month, whereas RI-3 failed after 14.4 ± 1.2 days. Micro-CT confirmed greater dimensional stability of P06 versus P08 lattices.

Significance: This work demonstrates that high-content PCL/β-TCP composites can be reliably 3D printed into stress-adaptive mandibular implants, and establishes quantitative design thresholds for balancing early mechanical support with degradation in oral and maxillofacial reconstruction.

1. Introduction

Segmental mandibular continuous defects exceeding the critical size are commonly resulting from trauma, tumors, or osteoradionecrosis. Fibula-free flap surgery (FFS) used with a traditional reconstruction plate is the gold surgical standard approach for reconstruction due to the large bone defect's inability to heal naturally [1–5]. However, this approach is associated with several challenges, such as prolonged operative time, extended recovery periods, and restricted restoration of anatomical morphology and function. Recently, patient-specific mandibular implants have been developed by integrating medical image processing, computer-aided design (CAD), and metal 3D printing, aiming to improve both aesthetic outcomes and biomechanical performance [6–8]. These implants effectively support the mandibular structure and maintain facial appearance, speech, and masticatory function. Nevertheless, permanent placement of metal implants can lead to complications such as stress shielding, corrosion, wear, infection, and difficulty in removal, which may adversely affect long-term clinical outcomes and overall patient quality of life [9–11].

Developing patient-specific biodegradable 3D-printed

* Correspondence to: Department of Biomedical Engineering, Medical Device Innovation and Translation Center,National Yang Ming Chaio Tung University, 112, No.155, Section2, Linong Street, Taipei, Taiwan.
E-mail addresses: qqandqq124@nycu.edu.tw (H.-W. Wang), cherryamigo46@nycu.edu.tw (C.-M. Chang), chengyen.be12@nycu.edu.tw (Y. Cheng), egidijus.simoliunas@gmc.uv.lt (E. Šimoliūnas), paoweilee.be11@nycu.edu.tw (P.-W. Lee), wayne.be11@nycu.edu.tw (W.-C. Tsai), cllin2@nycu.edu.tw (C.-L. Lin).

https://doi.org/10.1016/j.dental.2026.01.003
Received 29 August 2025; Received in revised form 8 January 2026; Accepted 8 January 2026
Available online 19 January 2026

reconstruction implants (RIs) with structural integrity and the ability to promote bone regeneration has become an important strategy for treating critical bone defects in the mandible [12–16]. However, the mechanical strength of biodegradable RIs is significantly inferior to that of metal materials. The initial stabilization period for bone defect reconstruction lasts approximately 4–6 weeks after surgery, during which bone osseointegration is not yet complete. During this period, the RIs fixed to the mandible must independently withstand the combined challenges of muscle traction, local tension, and the hydrolytic environment [7–11]. Micro-motion, cracks or fractures, and failure of bone osseointegration can severely compromise the stable support of external forces necessary for successful reconstruction. These issues often result from improper design or mismatched degradation kinetics of the biodegradable scaffold [17]. However, there is currently a lack of standardized guidelines regarding the design principles, structural mechanical stability, and early degradation mechanisms of 3D-printed biodegradable RIs for critical mandibular bone defects.

Compared to polylactic acid (PLA), the biodegradable polymer polycaprolactone (PCL) produces fewer acidic degradation byproducts, making it more favorable for bone cell regeneration [18–21]. However, PCL exhibits relatively low mechanical strength and high ductility, which limits its application in load-bearing scenarios. Many studies have demonstrated that incorporating β-tricalcium phosphate (β-TCP) significantly enhances the initial mechanical strength and osteoconductive properties of PCL, thereby making it more suitable for short-term or early-stage load-bearing scaffolds [19,22]. PCL/β-TCP composite filaments can also be processed using fused deposition modeling (FDM), an additive manufacturing technique that extrudes thermoplastic polymers in a controlled layer-by-layer manner to build complex structures [19,22]. FDM is particularly compatible with biodegradable materials such as PCL and PCL/β-TCP composites, allowing precise control over porosity, lattice geometry, and material distribution—factors that are critical for balancing mechanical stability with effective bone regeneration. These capabilities make FDM especially advantageous for fabricating customized biodegradable reconstruction implants tailored to the anatomical and functional requirements of segmental mandibular defects. However, 3D-printed solid reconstruction implants do not provide sufficient internal space to promote bone cell growth and angiogenesis. Creating a suitable lattice structure as the scaffold is important to provide places for cells to attach and pathways that help cells move in and build new bone [17]. The lattice size and pattern must balance structural stability and biodegradation control, especially during the early postoperative period (e.g., within the first month after surgery). Achieving a dynamic balance between mechanical support, hydrolysis rate, and regenerative guidance is crucial.

Although PCL+ β-TCP biodegradable materials have not yet been applied to load-bearing RIs, effective clinical application potential can be realized through lattice microstructure design optimization and postoperative load management [17,19]. To balance the mechanical stability in the early postoperative period with the material degradation rate, this study combines image processing, finite element (FE) analysis, and structural topology optimization. Patient-specific 3D-printed RIs with different critical size are performed for structural stress analysis under worst-case load conditions. A gradient lattice configuration is implemented, using small units and high-density lattices in high-stress areas to enhance local support and large-pore, low-density lattices in low-stress areas based on the stress distribution results. After printing fabrication, four-point bending tests were conducted to understand fundamental mechanical strength for RIs with different critical-size. Simultaneously, mechanical behavior observations of the implant under muscle traction and aqueous degradation were simulated on a phosphate-buffered saline (PBS) solution load platform with thermal environment.

Accordingly, patient-specific biodegradable implants composed of PCL reinforced with β-TCP were developed using FDM for the reconstruction of critical-sized mandibular defects. A gradient lattice design strategy was incorporated to systematically examine how lattice distribution and defect size affect early postoperative mechanical stability and the material's degradation thresholds. Through this combined evaluation, the study sought to establish quantitative design criteria that balance structural support with controlled biodegradation for reliable RI of mandibular critical-sized defects.

2. Materials and methods

Fig. 1 illustrates the workflow of this study. The process begins with the synthesis of PCL and β-TCP composite materials, followed by filament extrusion and the development of FDM 3D printing techniques. After material property evaluation, different RI models with topology-optimized lattice designs are fabricated. Mechanical testing was performed to understand their bending strength. A dual loading platform is employed to simultaneously simulate hydrolytic conditions and postoperative dynamic loading based on a standard degradation curve, allowing comprehensive assessment of the early-stage stability and degradation behavior of each design, which serves as a foundation for in vivo animal studies in the future.

2.1. Synthesis and composition analysis of PCL+ β-TCP materials

PCL (Ingevity UK Ltd, Warrington, UK) and β-TCP (Tokyo Chemical Industry Co., Ltd, Tokyo, Japan) were used to prepare composite filaments as biomedical materials for FDM 3D printing. The materials were mixed at a weight ratio of 7:3, and 450 mL of ethyl acetate (Cheng Yi Chemical Co., Ltd., Taipei, Taiwan) was added as a solvent to facilitate uniform blending. The mixture was treated with an ultrasonic oscillator (RBS FTD20, KUDOS, Shanghai, China) for 32 h (400 W, 40 kHz) to ensure thorough dispersion of the powder. It was then poured onto a glass plate and left in a fume hood for 8 h to allow complete evaporation of the solvent, followed by drying in an oven at 30°C for another 8 h. After drying, the material was cut into 5 mm square pieces using a knife and ground into powder using a grinder, resulting in an average particle size of less than 500 μm. The powder was further sieved to ensure consistency in particle size if necessary (Fig. 2(a)).

The resulting powder was fed into a filament extrusion machine (Filament Maker One, 3Devo Inc., Utrecht, Netherlands) for wire extrusion. The extrusion zone temperatures were set as follows: 75°C at the feed zone, 80°C in the middle heating zone, and 65°C at both the outlet zone and the nozzle end. The screw speed was maintained at 2.2 rpm to prevent material collapse before solidification. The side roller speed was adjusted to maintain a consistent filament diameter of 2.75 ± 0.05 mm during extrusion while confirming the absence of bubbles and foreign particles. The final filament was stored in a moisture-proof container with a relative humidity of 22 % for subsequent FDM printing (Fig. 2(a)).

2.2. Physicochemical and biocompatibility Analysis

After getting the printing filament ready, we used Gas Chromatography–Mass Spectrometry (GC-MS), Fourier Transform Infrared Spectroscopy (FTIR), and a cytotoxicity test (MTT assay) to check if the material is chemically stable and safe for biological use.

GC-MS analysis was performed to determine whether any residual volatile organic solvents or other potentially harmful compounds were present in the material. A total of 10 g of filament composed of 70 wt% PCL with 30 wt%β-TCP was ground into powder and analyzed as the test sample. The analysis was conducted using a thermo scientific trace 1300 GC system (Thermo Fisher Scientific, Waltham, MA, USA) equipped with an ISQ mass spectrometer and an auto-sampler (TriPlus RSH). A standard temperature program was applied according to instrument guidelines, and the resulting retention times (RTs) and mass spectra were compared against reference spectra from the NIST 2017 and Wiley

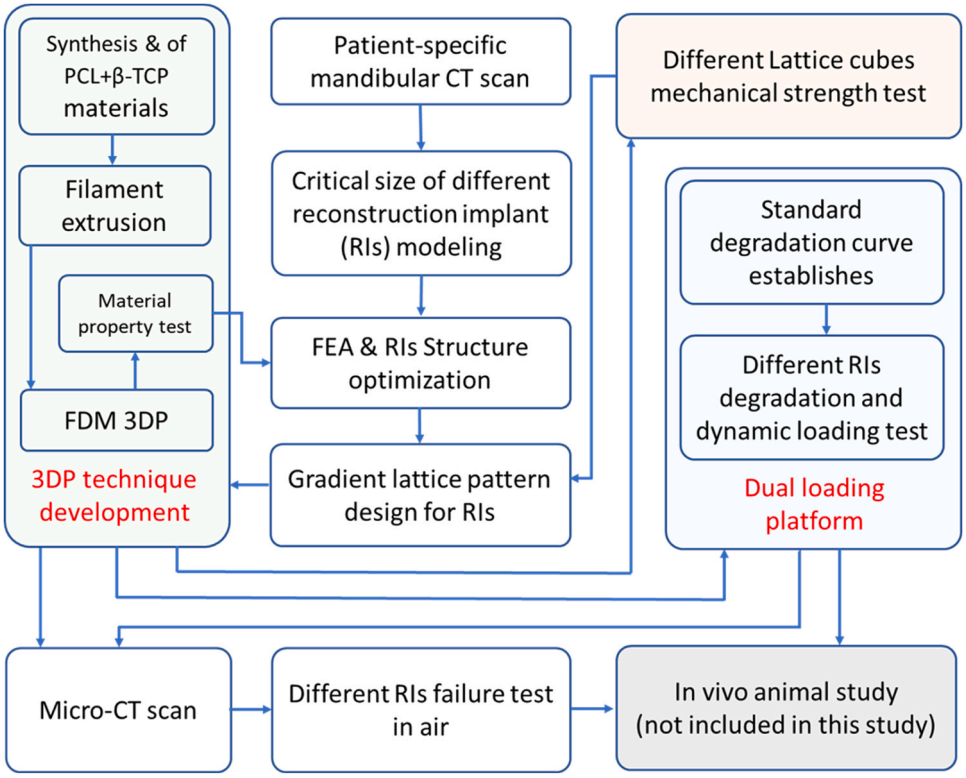

Fig. 1. Illustration of the workflow of this study.

10th Edition databases. This analysis aimed to verify whether the ethyl acetate used during material processing was fully evaporated and to detect any unexpected residual organic impurities.

FTIR spectroscopy (Jasco Inc., Easton, MD, USA) was employed to verify the presence of characteristic functional groups in the composite material, such as the ester carbonyl group (C═O stretching, ~1720 cm^{-1}) of PCL and the phosphate group (PO_4^{3-}, ~1040 cm^{-1}) of β-TCP. Additionally, FTIR was used to assess any potential chemical interactions or decomposition phenomena within the composite. FTIR analysis was conducted using a Jasco FTIR-4600 spectrometer. Three types of samples were analyzed: pure PCL, pure β-TCP, and the composite containing PCL with 30 wt% β-TCP. For each sample, 500 mg was prepared as a potassium bromide (KBr) pellet using the standard compression method. Spectra were recorded over the wavenumber range of 4000–400 cm^{-1} with a resolution of 4 cm^{-1} .

An MTT assay was performed to evaluate the cytotoxicity of material extracts according to ISO 10993 guidelines [23]. L929 mouse fibroblast cells and MG-63 human osteosarcoma cells were seeded in 96-well plates at a density of 1×10^5 cells/mL (100 μL/well) and incubated at 37 ± 1 °C in a humidified atmosphere with 5 ± 1 % CO_2 for 24 ± 2 h to allow cell attachment. Test samples were sectioned into small pieces and extracted in Dulbecco's Modified Eagle Medium (DMEM; Gibco, Thermo Fisher Scientific, USA) at a surface weight-to-volume ratio of 0.2 g/mL for 24 h at 37 °C. Cells were then treated with 100 % or 50 % extract or control medium for an additional 24 h. All treatments were conducted in triplicate. After exposure, 100 μL of MTT solution (0.5 mg/mL; Apolo Biochemical, USA) was added and incubated for 2 h to allow the formation of formazan crystals. The crystals were dissolved in 100 μL of dimethyl sulfoxide (DMSO; Sigma-Aldrich, USA), and absorbance was measured at 570 nm using a microplate reader (TECAN Sunrise, Tecan Group Ltd., Switzerland). Cell viability was calculated relative to the negative control, with values below 70 % considered cytotoxic.

2.3. *Mechanical property test of PCL+ β-TCP materials*

To obtain accurate material properties for RIs to be used in subsequent FE analysis, tensile testing was performed to determine the elastic modulus (Elastic modulus) and Poisson's ratio of the PCL+ β-TCP composite. The specimen design followed the ASTM D638 standard [24], with a total length of 80 mm, a gauge length of 50 mm, and an effective deformation region of 25 mm (width: 9 mm; thickness: 3 mm). Specimens were fabricated using a 3D FDM printer (Fig. 2(b)) [16]. The PCL+ β-TCP composite was made into standard 3D printing filaments that are 2.85 mm wide, following the earlier steps to make sure they work with the FDM printer (S7, Ultimaker, Geldermalsen, Netherlands).

The printing parameters were as follows: nozzle temperature of 155°C, bed temperature of 40°C, printing speed of 20 mm/s, layer height of 150 μm, and 100 % infill density. Three replicate specimens were printed for each material group. After printing, all samples were conditioned in a controlled environment at 23°C and 50 % relative humidity for 24 h to relieve internal residual stresses and minimize stress concentrations that could affect the testing outcomes. An extensometer (HT-9160, Hung Ta Instrument, Taiwan) was carefully clamped onto the gauge section of each specimen to ensure stable contact and to prevent slippage or misalignment during testing. Additionally, transverse strain gauges were attached to measure lateral deformation, enabling the calculation of Poisson's ratio. Specimens were mounted between the upper and lower grips of a universal testing machine (E3000, Instron ElectroPuls®, Instron, Canton, MA, USA). The tensile test was conducted at a crosshead speed of 5 mm/min with an initial preload of 10 N. Longitudinal strain, transverse strain, and tensile stress were recorded throughout the test. Testing was monitored to ensure deformation behavior was consistent with expected material characteristics. Each test was terminated upon specimen failure or after reaching maximum elongation. Data analysis focused on determining the elastic modulus and Poisson's ratio.

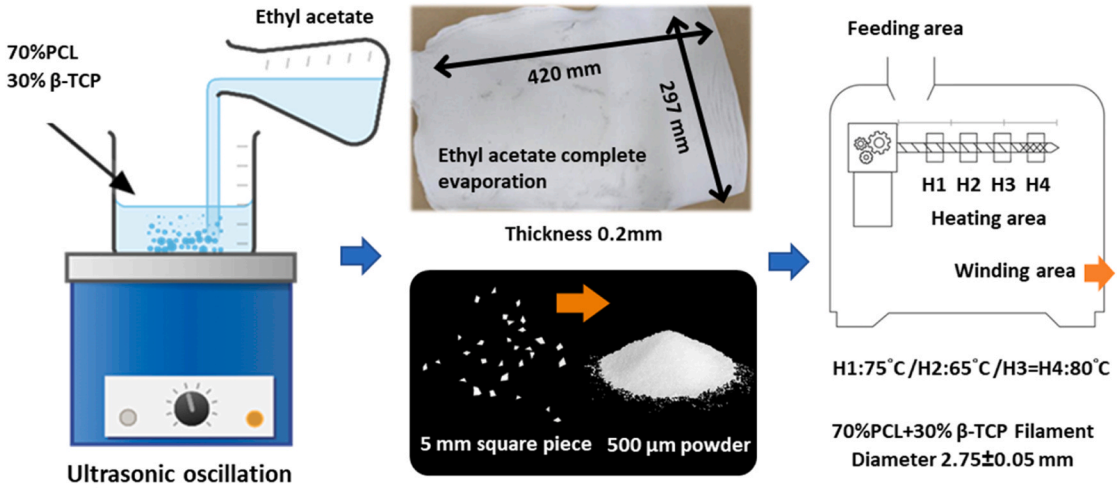

(a)

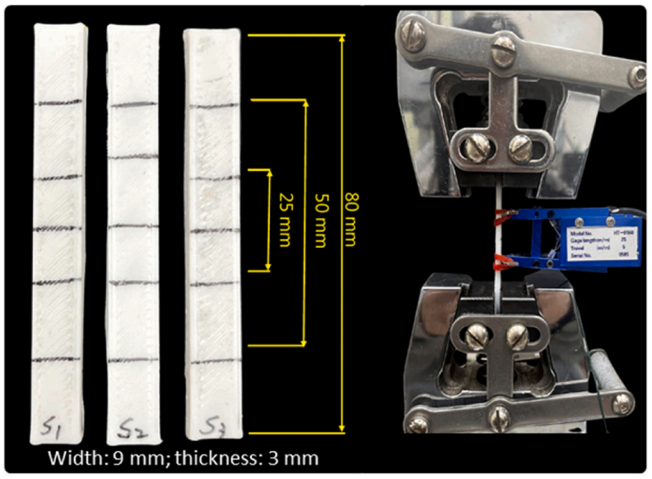

	Elastic modulus (MPa)	Poisson's ratio	Elongation
1	447.75	0.33	3.54
2	450.46	0.25	3.60
3	484.74	0.31	2.84
Ave.	450.40	0.30	3.33
Std.	20.62	0.03	0.42

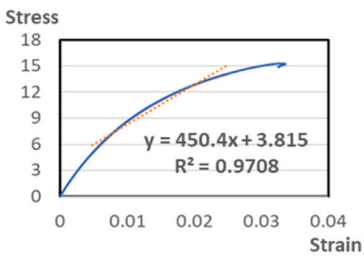

(b)

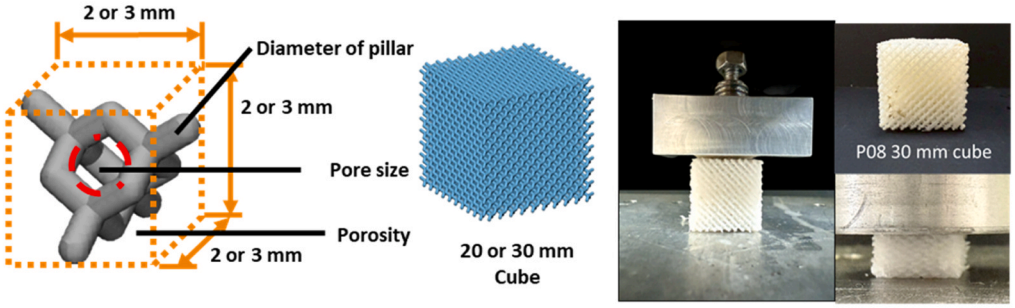

Diamond	Unit size (mm)	Pore size (μm)	Porosity (%)	Pillar diameter (mm)
P06	2	1000	65	0.6
P08	3	1650	70	0.8

(c)

Fig. 2. (a) Mixing and filament extrusion process of PCL and β-TCP. Left: Prolonged ultrasonic agitation for thorough mixing; Middle: Solvent evaporation using ethyl acetate; Right: Schematic of filament extrusion and corresponding temperature settings. (b) Left: 3D-printed samples fabricated according to ASTM D638 standard; Middle: Tensile testing setup; Right: Resulting data and stress-strain curves. (c) Left: Diamond-shaped lattice structure; Middle: CAD model; Right: Printed diamond lattice cube and schematic of compressive strength testing.

2.4. Mechanical strength test of 3D-printed PCL+ β-TCP lattice cube structures

Mechanical strength tests were conducted on cube-shaped structures measuring 20 mm and 30 mm, which included different diamond lattice designs (P06-dense lattices and P08-larger pores), while applying pressure to them. Fig. 2(c) summarizes the unit size, pore size, porosity, and pillar diameter of the two lattice types. Specimens (n = 3 per group) were fabricated using the previously described FDM 3D printing process, following the same printing parameters established in the material property tests. After fabrication, specimens were conditioned using the same stabilization procedures previously described.

Compression tests were performed with an E3000 testing machine that had flat, strong plates to keep the samples from moving sideways. The loading rate was set at 5 mm/min, and the compressive failure force (N) was recorded when the upper platen reached a displacement of two-thirds of their original height (Fig. 2(c)).

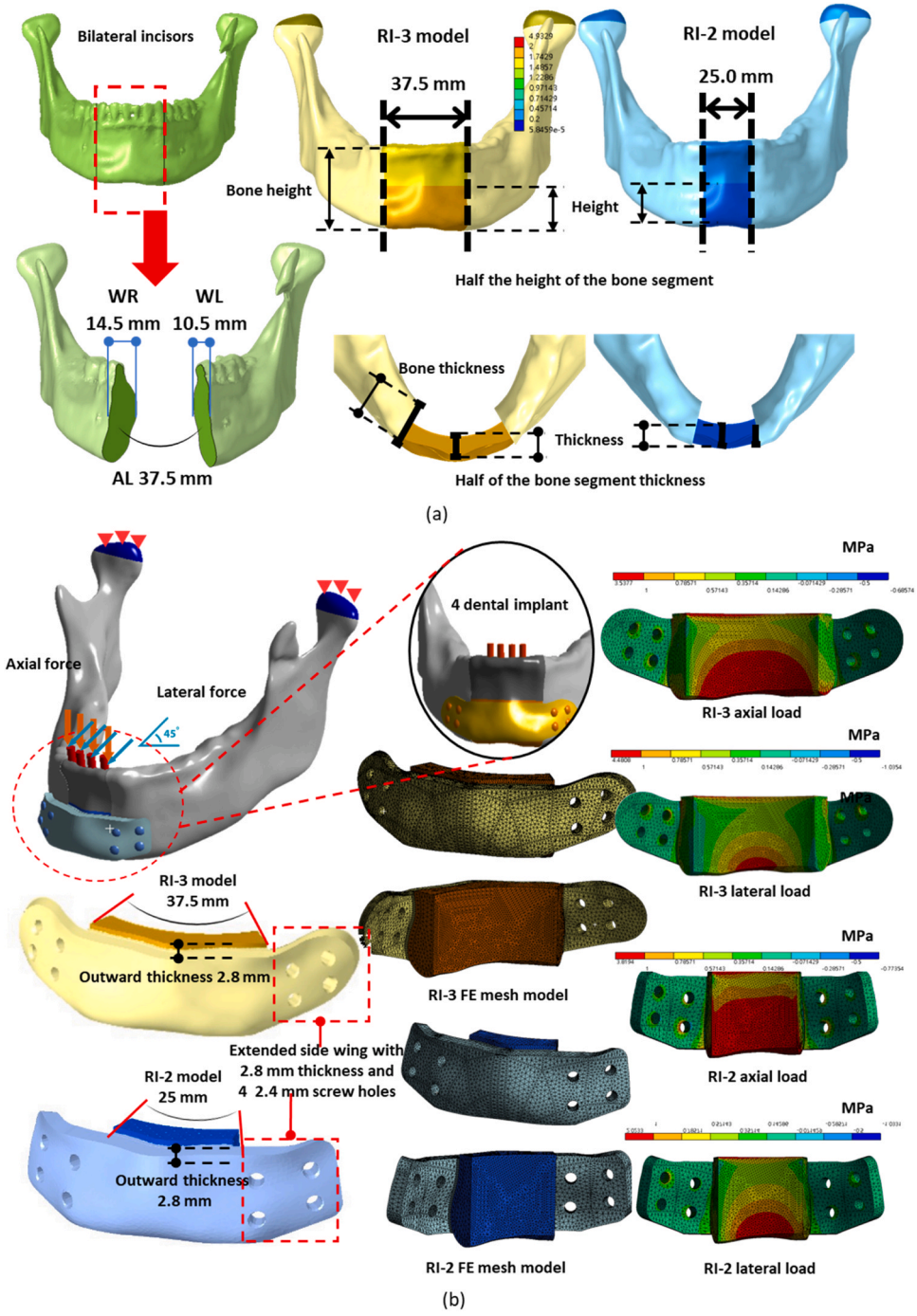

Fig. 3. (a) Definition of two types of critical bone defects located between the bilateral incisors and the widths of the two cross-sections (WR = 14.5 mm, WL = 10.5 mm) correspond to two and three times the average mesiodistal width between the canines and first premolars, respectively. Both the height and width of the defects were set to half the original alveolar ridge dimension. (b) Top left: Schematic illustration of loading conditions applied to four dental implants after mandibular anterior defect reconstruction, consisting of lateral (70 %) and axial (30 %) forces; Bottom left: CAD models of the two implant designs, RI-2 and RI-3; Middle: Corresponding full-view finite element (FE) mesh models; Right: FE analysis results showing maximum principal stress distribution for the two models.

2.5. FE analysis and topological optimization of the mandibular segmental reconstruction implant

A digital mandible model with a standardized segmental defect located between the bilateral incisors, including the incisors and canines, was constructed from a normal male patient's computed tomography (CT) scan data and was used in our previously established CAD model [6]. We measured the arc length distance (AL=37.5 mm) and the widths of the two cross-sections (W*R*=14.5 mm, WL=10.5 mm) between the bilateral premolar and canine sections at half the occlusal height. It was found that AL is approximately three times the average value of the sum of W*R* and WL (12.5 mm); thus, it is defined as RI-3. The design of RI-3 is based on the guidelines from earlier metal implants, which include making the implant height half the height of the bone segment, the implant thickness also half of the bone segment thickness (Fig. 3(a)), adding an arc normal outward and extended side wing that is 2.8 mm thick, and including 4 holes for 2.4 mm bone screws to secure it [5,6] (left part in Fig. 3(b)). Using the method described, a new set of implants called RI-2 is created by reflecting in the sagittal plane, and this implant had an arc length that is double the average of W*R* and WL (about 25 mm)(Figs. 3(a) and 3(b)).

Solid models of the RI-2 and RI-3, along with the corresponding fixation screws, bone graft (autogenous bone-cortical bone equivalent), and remaining mandibular segments, were imported into ANSYS Workbench (ANSYS Workbench v18.2, ANSYS Inc., PA, USA) for simulation. Numerical mesh convergence tests were performed for both RI-2 and RI-3 using four different tetrahedral element sizes. A vertical load of 100 N was applied to the occlusal surfaces of the premolar regions on both sides as the loading condition, while the nodes on the condyles were fully constrained in all directions to represent the boundary conditions. The elastic modulus and Poisson's ratio of cortical bone, cancellous bone, and fixation screw were assigned according to values reported in the literature (Table 1) [6]. The maximum principal stress in the remaining bone surrounding the implant was used as the convergence indicator. Convergence was considered achieved when the stress variation between mesh densities was less than 5 %. Table 2 summarizes the number of nodes/elements, stress values, and corresponding error percentages for the RI-2 and RI-3 models. The results indicated that both models reached convergence at an element size of 1 mm; therefore, this mesh density was adopted for all subsequent analyses.

Weighted topology optimization was performed to develop lightweight and mechanically strengthened internal structures for RI-2 and RI-3. Four solid dental implants (3 mm × 15 mm) were inserted into the segmental bone grafts at the lateral and central incisor positions to simulate the postoperative occlusal loading transferred from a temporary prosthesis (Fig. 3(b)).

Mesh-converged FE models were used for optimization. The design domain included only the RI region, while the outer and extended wing portions were excluded. Two loading conditions (100 N each) were applied to represent early anterior mandibular function: (1) an axial biting load and (2) a 45° lateral load. The condyles were fully

Table 1
Elastic modulus and Poisson's ratios of all materials simulated using finite element analysis.

Material	Elastic modulus (GPa)	Poisson's ratio	Reference
Cortical bone	13.70	0.30	[6]
Cancellous bone	1.37	0.30	[6]
Titanium implant	110.00	0.35	[6]
Fixation screw (Ti6Al4V)	110.00	0.35	[6]
Autogenous bone (cortical bone equivalent)	13.70	0.30	[6]
PCL+ 30 % ß-TCP	0.45	0.30	Study testing

Table 2
A 1.0-mm element size achieved mesh convergence for both RI-2 and RI-3.

RI-2 Element size (mm)	Node number	Element number	Maximum principal stress (MPa)	Percentage error (%)
1	1579665	1023991	124.39	0
1.1	1471288	941523	119.17	3.76
1.2	1425526	906630	106.45	14.42
1.5	1404250	890297	80.0	30.86
RI-3				
1	1606245	1012226	60.32	0
1.5	1439638	885164	60.31	0.02
2	1435382	881857	58.86	2.43
2.2	1434599	881240	48.61	19.41

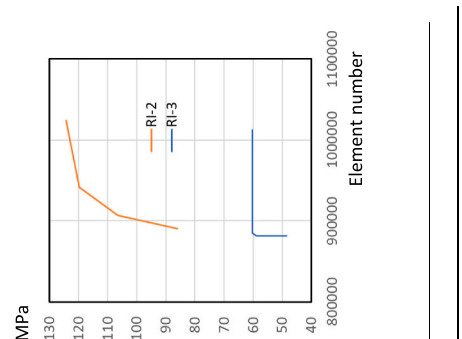

constrained for both load cases. For each load case, element-wise compliance was computed (C_{axial} and $C_{lateral}$). These values were used by the solver to update the density design variable rather than being normalized. Because anterior defects mainly experience lateral shear, weighting factors of 0.7 (lateral) and 0.3 (axial) were assigned. The optimization objective was to minimize the weighted compliance:

$$C_{weighted} = 0.7\ C_{lateral} + 0.3\ C_{axial}$$

Element density (ρ=0–1) served as the design variable under a 50 % volume-retention constraint. Through iterative updates, elements essential for carrying the weighted loads were assigned higher density, while less critical elements were reduced. Based on the final density distribution, elements were classified as remove (0.0–0.4), marginal (0.4–0.6), or keep (0.6–1.0) regions (Figs. 4a and 4b). The resulting topologies for RI-2 and RI-3 were then smoothed to generate the final optimized core structures.

2.6. Gradient lattice pattern design, fabrication and precision test for reconstruction implant

The gray triangular grid positions in the left parts of Figs. 4(a) and 4(b) are the places where the structure must be kept. The yellow dot circles in the left part of Figs. 4(a) and 4(b) show that the shape of the RI-2 and RI-3 models (excluding the extended wing) after weighted topology optimization with keep, marginal, and removed regions. The right parts of Figs. 4(a) and 4(b) showed the gradient lattice patterns in the RI-2 and RI-3 models. The P06 lattice was used for the layout of the Keep region, which is the area where the implant experiences higher stress (from the right part in Fig. 3(b)). The removed and marginal regions refer to the areas where the implant experiences lower stress; P08 lattice was employed for their layout. The arc outward and two extended side wings are kept solid in Figs. 4(a) and 4(b). The 10-node tetrahedral element with 0.6 mm size was used to mesh the lattice for RI-2 and RI-3 models. After meshing, under the same boundary conditions as convergence test described, a downward bite force of 100 N was simulated at the first molar region on both sides of the RI-2 and RI-3 models. This force does not represent the actual occlusal force after sugery but rather indicates the potential maximum load resulting from mandibular muscle traction (Fig. 4(c)).

Using the same FDM 3D printing technology to fabricate the reconstruction implant samples. The model slicing operation was completed using Cura software (Ultimaker, Geldermalsen, Netherlands), and the same printing parameters as before were set for 3D printing. After printing, the implant samples clearly exhibited detailed lattice areas and structurally intact edge features, demonstrating good structural reproducibility and molding accuracy. The subsequent samples will be used for geometric accuracy analysis and biomechanical experiments (Fig. 5(a)).

To evaluate the geometric dimensional accuracy of 3D printed RIs, this study uses micro-computed tomography (micro-CT) (U-CTHR, MILabs B.V., Houten, The Netherlands) with 40μm resolution to scan and reconstruct the printed products, generating corresponding 3D surface models. Compare the micro-CT reconstructed model with the original CAD design to analyze the potential geometric deviations that may occur after printing. This study measures the dimensions of three samples each of the RI-2 and RI-3 models, including total dimensions (total width: TW; total height: TH), geometric dimensions of the lattice area (lattice width: LW, lattice height: LH), and the diameter of the screw holes (selecting one lock hole on each side to measure the hole diameter: HD) (Figs. 5(b) and 5(c)). The lattice areas of the models are subjected to cross-sectional analysis at three representative sections (Sections 1, 2, 3), with the positions of each section evenly divided by angle (12.5° for RI-2 and 12.5° for RI-3). In each section, lattice pores designed with diameters of P06 and P08 are selected for measurement, and their differences from the original CAD model are compared. Through the aforementioned geometric measurements and comparisons, the accuracy and potential deformation of the printed products in different sizes and areas can be systematically evaluated (Figs. 5(b) and 5(c)).

2.7. Four-point bending test of reconstruction implant in air

To provide a comprehensive mechanical strength reference for RIs in the air condition, four-point bending tests were carried out for RI-2 and RI-3 models according to the American Society for Testing and Materials (ASTM) protocols (ASTM F382–17), using the Instron E3000 testing machine.

Static testing was performed to obtain the proof load and strength of the samples. The rigid extension segments, which are used to effectively lengthen the RI-2 and RI-3 models, do not have a sufficiently long symmetrical section. The geometry profile at the proximal and distal sides of the rigid extension segments for the RIs were designed according to their corresponding geometric features of the implants and fabricated using an ABS 3D printer (ABS-P430; Dimension 1200es SST, Stratasys, Ltd., Minnesota, USA). All RI samples were attached to the rigid extension segments, and the loading rollers touched these segments during the test (Fig. 6(a)).

The center span (a=100 mm) is the distance between the loading rollers, and the loading span distance (h=35 mm) is the distance between the loading roller and the nearest support roller. Each group had three samples, which were placed on the four-point bending test clamp to load at a crosshead rate of 5 mm/min until failure occurred (Fig. 6(a)). The proof load (P), and force-displacement diagram were collected from each test, and the corresponding bending strength was calculated. The failure pattern of each sample was examined to assess the failure mechanism.

2.8. Standard degradation curve establishes under simulated oral physiological conditions

To establish a standard degradation curve for PCL+ β-TCP materials under simulated oral physiological conditions, a custom experimental platform equipped with heating and mechanical loading functions was developed. The setup consisted of PBS maintained at 37°C and pH 7.4 and was integrated with a dynamic mechanical testing system (E3000). In the experiment, a 20 mm cube made of diamond lattices (with each unit size being 2 mm and the pillar diameter being 0.6 mm: P06), created using the same FDM 3D printing and was placed between the loading device and the grip to fully submerged in PBS (Fig. 7(a)).

The testing protocol employed a bi-daily cyclic compression mode, applying a reciprocating compressive load ranging from 5 to 50 N for a duration of 20 min per session (approximately 1370 cycles at 1.142 Hz, simulating 1 million occlusal cycles annually) [25,26]. This loading pattern was designed to simulate minor occlusal forces or muscle tension that may occur after surgery. Between cycles, samples were left undisturbed for 11 h and 40 min to mimic a rest period. A preload of 5 N was applied at the start of each cycle to ensure stable contact and consistent alignment of the specimen (Fig. 7(a)).

Degradation was assessed at 24 (1 day), 72 (3 days), and 168 (7 days) hours. At each time point, three specimens were collected, rinsed, dried, and weighed to determine mass loss. In addition, the pH of the PBS solution was recorded at the beginning and end of each testing period to monitor whether the degradation process altered the environmental acidity or alkalinity.

2.9. Hydrolytic degradation with dynamic loading test

To simulate the combined effects of muscle traction and physiological degradation on RIs during the early postoperative period, dynamic loading tests were conducted using a previously established experimental platform.

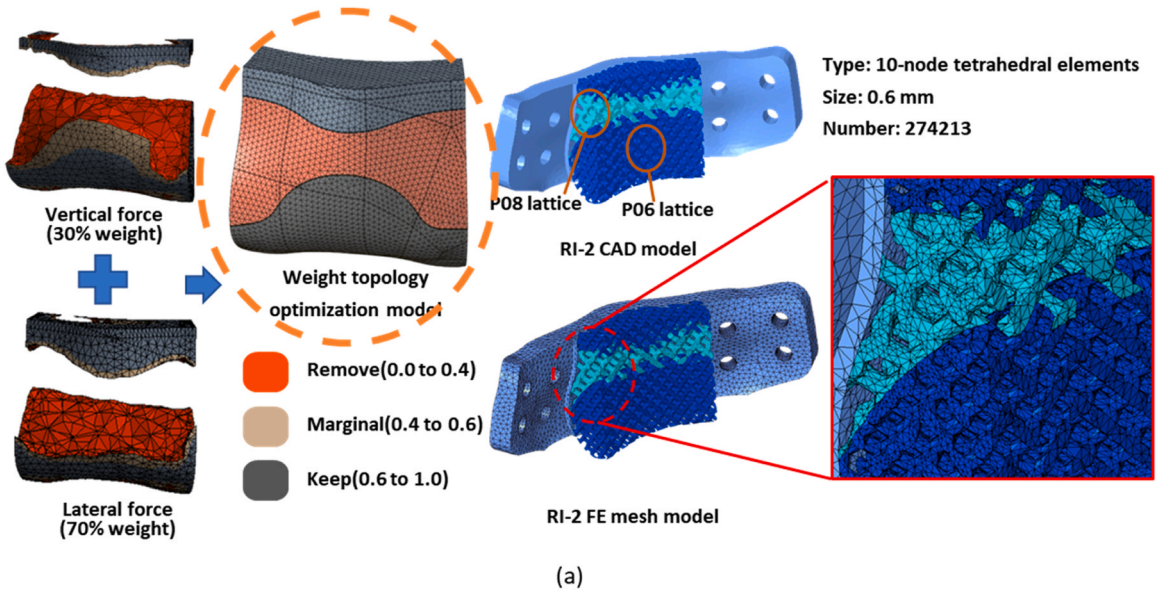

(a)

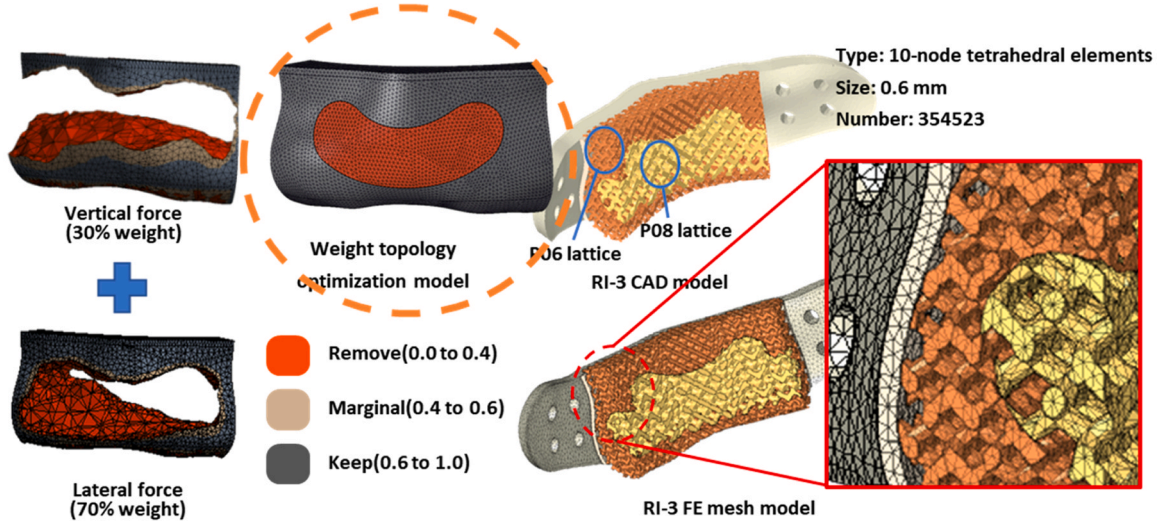

(b)

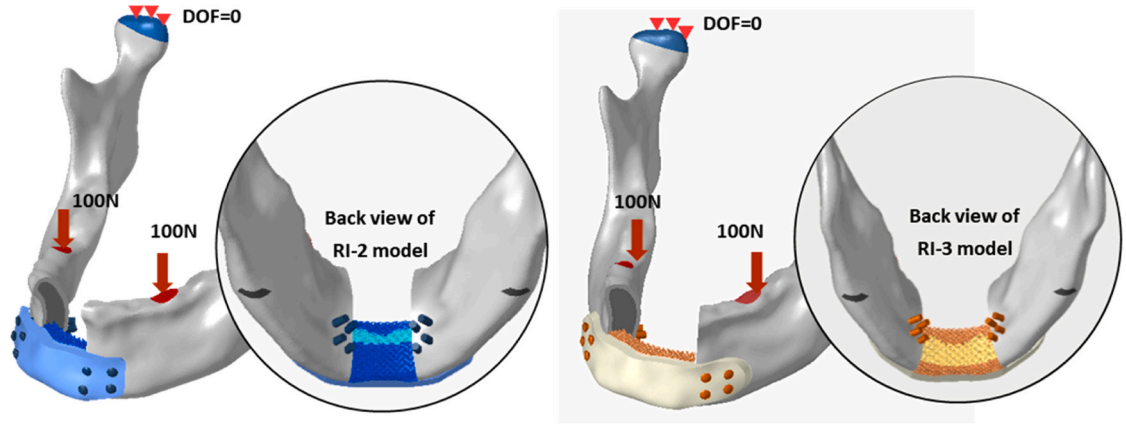

(c)

Fig. 4. (a) Left: Topology-optimized structures of the RI-2 model under axial and lateral loading conditions, with the kept element regions indicated. The yellow dot circles highlight the areas refined by weighted topology optimization and subsequent smoothing. Right: Regions defined as "keep" and "remove" elements were filled with P06-dense lattice and P08-larger pore structures, respectively, along with the corresponding FE mesh model; (b) Left: Topology-optimized structures of the RI-3 model under axial and lateral loading conditions, with the kept element regions indicated. The orange dot circles highlight the areas refined by weighted topology optimization and subsequent smoothing. Right: Regions defined as "keep" and "remove" elements were filled with P06 and P08 structures, respectively, along with the corresponding FE mesh model; (c) FE simulation for RI-2 and RI-3 models under load.

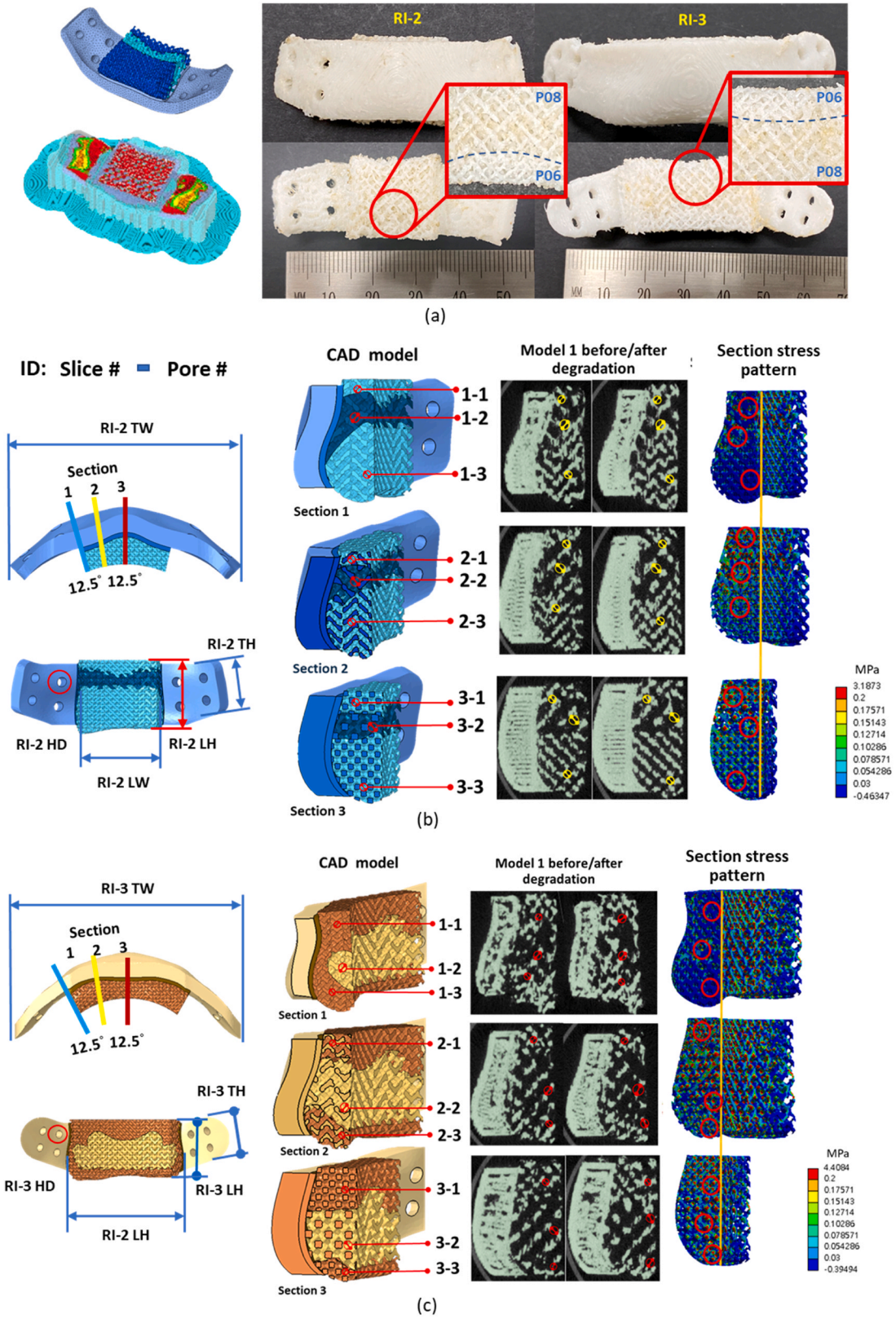

Fig. 5. (a) Left: Model slicing and conversion for input into 3D printing software. Right: FDM (fused deposition modeling) 3D-printed RI-2 and RI-3 models, clearly showing the different lattice densities of P06-dense lattice and P08-large pore structures; (b) Left: Overall dimensional inspection of the RI-2 model. Right: micro-CT scan of nine pores across three cross-sections before and after hydrolysis (refer to Table 3), along with FE analysis stress distribution on the same cross-sections; (c) Left: Overall dimensional inspection of the RI-3 model. Right: micro-CT scan of nine pores across three cross-sections before and after hydrolysis (refer to Table 3), along with FE analysis stress distribution on the same cross-sections.

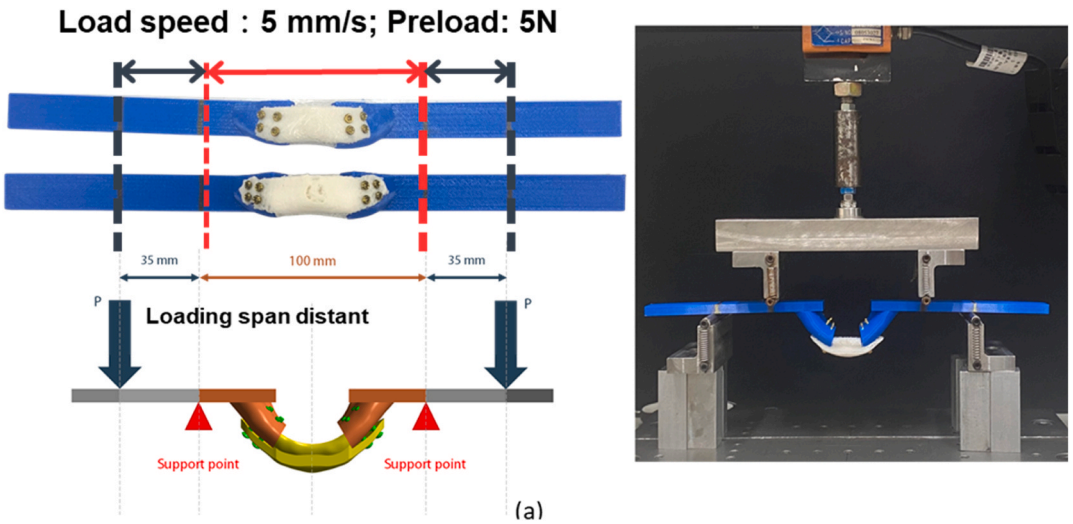

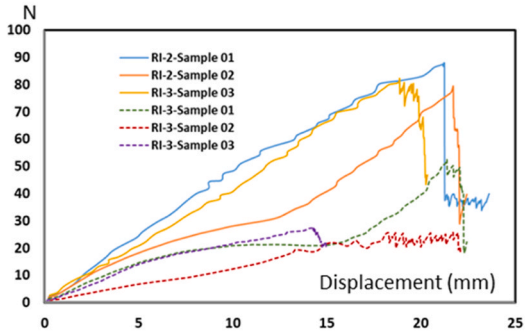

Sample No.	Proof load (N)	Bending strength (N*m)
RI-2 Sample 01	89.60	1568.00
RI-2 Sample 02	79.40	1389.50
RI-2 Sample 03	82.25	1439.38
Ave.±Std.	83.75±5.26	1465.63±92.10
RI-3 Sample 01	52.4	917.00
RI-3 Sample 02	26.73	467.69
RI-3 Sample 03	28.05	490.88
Ave.±Std.	35.73±14.46	625.19±252.98

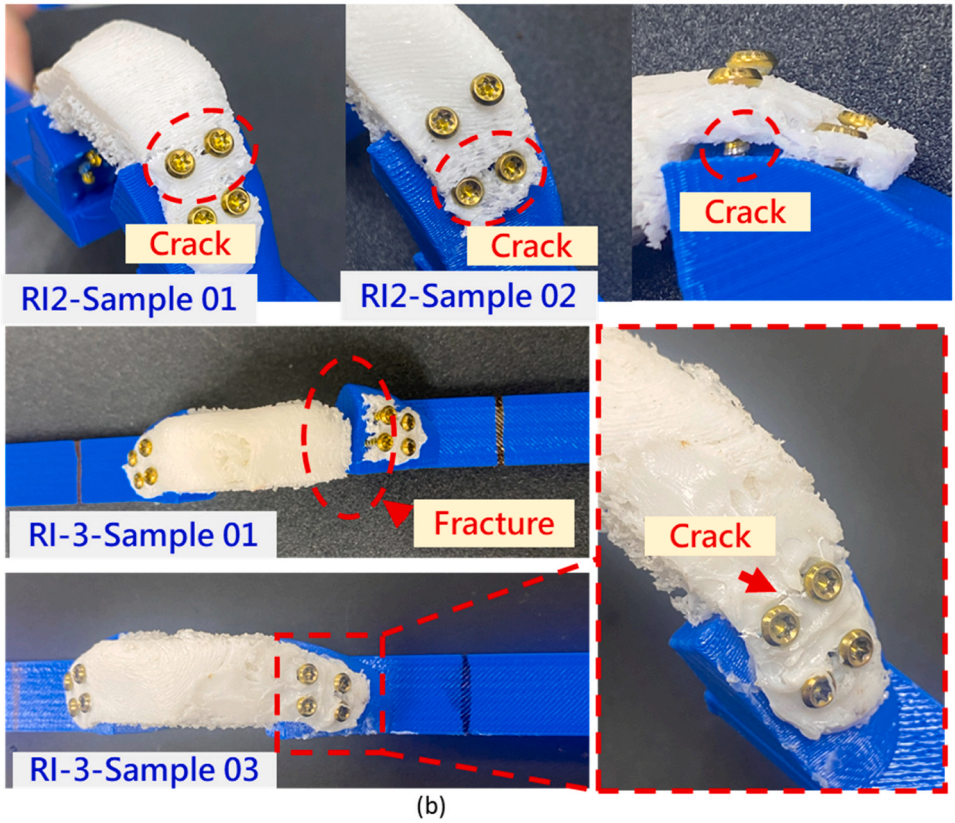

Fig. 6. (a) Schematic diagram of the four-point bending test;(b) Top left: Load–displacement curve from the four-point bending test. Top right: Proof load and bending strength values. Bottom: Crack and fracture locations of RI-2 and RI-3 models.

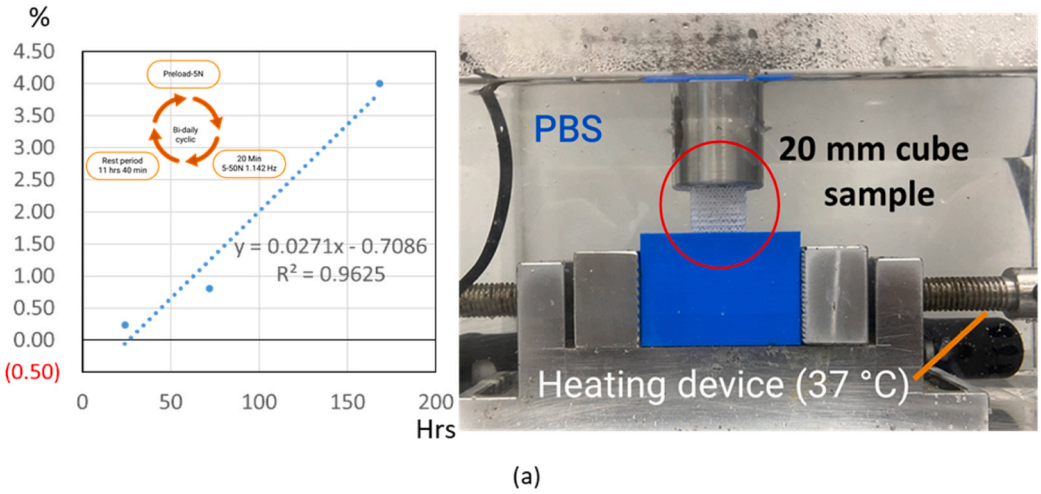

(a)

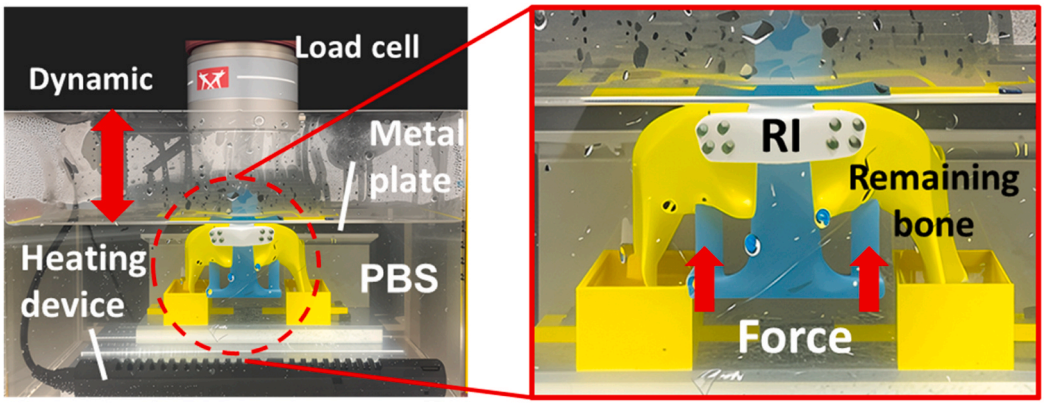

(b)

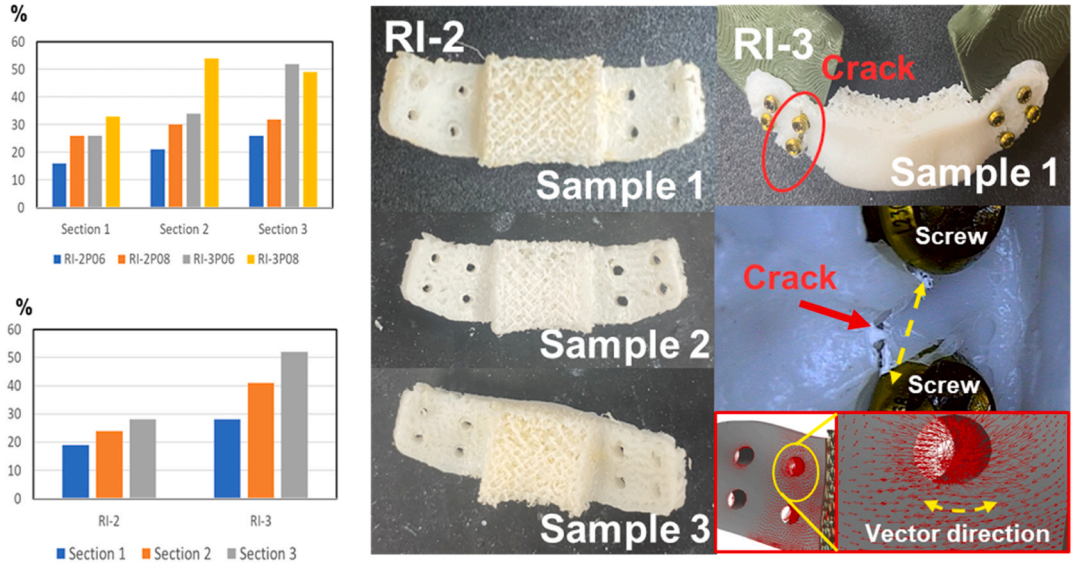

(c) (d)

Fig. 7. (a) Schematic diagram illustrating the establishment of a standard degradation curve and the corresponding plot of weight loss percentage versus actual time; (b) Setup and schematic diagram of the dual-loading platform for hydrolytic degradation with dynamic loading; (c) Left: Percentage change in geometry across different cross-sections and pores of RI-2 and RI-3 after dual loading; (d) Left: No cracks or fractures were observed in the RI-2 samples after one month. Right-top: Representative RI-3 sample showing crack/fracture after 14.4 days. Right-middle: Crack propagation path observed under an optical magnifier. Right-bottom: FE-predicted maximum principal stress directions around the pore regions.

For sample preparation, the remaining mandible segments corresponding to the RI-2 and RI-3 designs were fabricated using an ABS 3D printer. The 3D-printed PCL+ β-TCP RIs were secured onto the ABS mandible models using screws (Tandry Locking Bone Plate System, φ2.4 mm diameter, 18 mm length, Microware Precision Co., Ltd., Taiwan), forming the complete test samples. During testing, each sample was mounted in an inverted position on a dynamic testing machine (Instron E3000). The condylar processes were embedded and fixed in resin blocks to ensure positional stability. Following the protocol described by Wiebke Schupp and other researchers [25,26], a custom metal pressure plate was placed above the mandibular angle region to restrict undesired movement. A specially designed metal loading apparatus was positioned beneath the bilateral alveolar regions (approximately at the first molar sites) to apply a cyclic upward force simulating muscle traction, with a load range of 20–200 N and a loading span of 47 mm (Fig. 7(b)).

All samples were immersed in PBS at 37°C to replicate the humid and thermally stable in vivo environment. Initially, three RI-2 samples were subjected to dynamic loading at 1 Hz for 20,000 (about 5.5 h) cycles (Table 3). After testing, the implants were dried, and the mass loss due to hydrolysis was recorded. The results were compared with a previously established standard degradation curve (real time) to estimate the equivalent oral functional time, calculated to be 42.63 h. Accordingly, the extrapolated cumulative functional time in the aqueous environment for the first postoperative month (720 h) was determined to correspond to 93 h of in vitro fatigue exposure (Fig. 7(b)).

Subsequently, three sets each of RI-2 and RI-3 samples were subjected to 93-hour dynamic loading in PBS at 37°C under the same 20–200 N cyclic load conditions. Upon completion, all samples were UV-dried for two hours and weighed. Visible cracks and fracture sites were recorded. Finally, micro-CT scanning was performed, and the reconstructed images were used to assess geometric changes by calculating the percentage difference in key structural features before and after dynamic testing.

3. Results

3.1. Physicochemical and biocompatibility analysis

The GC-MS analysis results show that the PCL + 30 % β-TCP sample and the blank group exhibit several characteristic peaks at RT (Retention Time) 4.71, 5.63, 8.97, and 15.98 min in the chromatogram (Fig. 8(a)). After comparing its retention time with the NIST and Wiley standard databases, no major characteristic peak corresponding to ethyl acetate was found, indicating that the solvent used during the preparation process has completely evaporated, with no significant residual volatile organic compounds. Overall, the material meets the volatile safety requirements for biomedical applications.

The FTIR analysis results show that the spectrum of the PCL + 30 % β-TCP composite material retains the characteristic absorption peaks of both pure PCL and pure β-TCP. PCL exhibits a distinct ester group (C═O) stretching vibration absorption peak at approximately 1720 cm^{-1} , while β-TCP corresponds to the symmetric and asymmetric stretching vibrations of phosphate groups (PO_4^{3-}) in the range of approximately 1040 cm^{-1} . These characteristic absorption peaks in the spectrum of the composite material still exist, and no significant new peaks are observed, indicating that the interaction between PCL and β-TCP is primarily physical mixing, with no significant chemical reactions occurring (Fig. 8 (a)). This result indicates that the material preparation process (including organic solvent treatment and high-temperature melting mixing) did not cause any changes in the component structure, demonstrating good compositional stability.

MTT cytotoxicity analysis showed that L929 fibroblasts maintained an average viability of 86 % ± 9.4 % under both the undiluted and 1/2 diluted extract conditions, exceeding the ISO 10993cytotoxicity threshold of 70 %. Similarly, MG-63 osteosarcoma cells exhibited viabilities of 83 % (100 % extract) and 90 % (50 % extract), both comparable to the untreated control group (100 %). All viability values remained above 70 %, demonstrating the absence of extract-induced cytotoxicity in both fibroblastic and osteogenic cell models. Together, these results indicate that the composite material exhibits favorable biocompatibility and is suitable for biomedical implant applications (Fig. 8a).

3.2. Mechanical property and strength of PCL+ β-TCP materials and its lattice cube structures

The elastic modulus and Poisson's ratio of PCL+ β-TCP were determined to be 450.4 ± 20.26 MPa and 0.3 ± 0.03 (mean ± standard deviation), respectively (Fig. 2(b) and Table 1). It was also observed that the elongation of PCL+ β-TCP was about 3.33 %. The average strength of 3D-printed PCL+ β-TCP lattice samples refers to the stress values measured during displacement-controlled compression tests, specifically when the cube samples were compressed to two-thirds of their original height. The results showed that the P06 cube exhibited greater strength (3.17 ± 0.53 MPa) compared to the P08 cube (1.33 ± 0.33 MPa), and this difference was statistically significant regardless of the material type or loading method (Fig. 2(c)).

3.3. FE simulation of RI-2 & RI-3 models

The right part of Fig. 3(b) presents the analysis stress results for the RI-3 and RI-2 topology optimizations under lateral and axial loads. Based on these results and weighting calculation, the structural optimization of the implant according to stress distribution, as well as the placement and mesh pattern of the P06 and P08 lattice designs, can be determined (Figs. 4(a) and 4(b)). These details have already been described in Section 2.5 and will not be repeated here.

The simulation results of the RI-2 and RI-3 models, after being designed with a gradient lattice pattern, showed that both designs exhibited evident stress concentrations (red-orange regions) around the screw holes of the extended wings (Fig. 8(b)). Moreover, examination of the maximum principal stress vectors around the pore regions in Fig. 7 (c) revealed that the stress directions were predominantly tangential to the circular holes. This observation explains why the cracks observed in Fig. 7(c) propagated radially from the hole edges. In addition, the lattice

Table 3
Comparison of the printing accuracy errors between the printed and CAD-designed dimensions for the three RI-2 and RI-3 models after micro-CT scanning.

	RI-2					RI-3				
	TW	**TH**	**LW**	**LH**	**HD**	**TW**	**TH**	**LW**	**LH**	**HD**
CAD	50.78	16.16	16.82	17.69	2.40	62.59	16.64	16.18	26.50	2.40
3DP Model (1)	50.74	15.74	16.16	16.77	2.33	62.67	15.87	15.76	26.15	2.25
3DP Model (2)	50.62	15.82	16.25	17.39	2.36	62.42	15.84	15.86	26.75	2.34
3DP Model (3)	50.38	15.99	16.13	16.86	2.32	62.43	15.73	15.74	26.72	2.32
Average	50.58	15.85	16.18	17.01	2.34	62.51	15.81	15.89	26.54	2.30
Standard deviation	0.18	0.13	0.06	0.34	0.02	0.14	0.07	0.06	0.34	0.05
Error (%)	-0.39	-1.91	-3.80	-3.86	-2.64	-0.13	-4.99	-1.79	0.15	-4.03

TW = total width; TH = total height; LW = lattice width; LH = lattice height; HD = hole diameter.

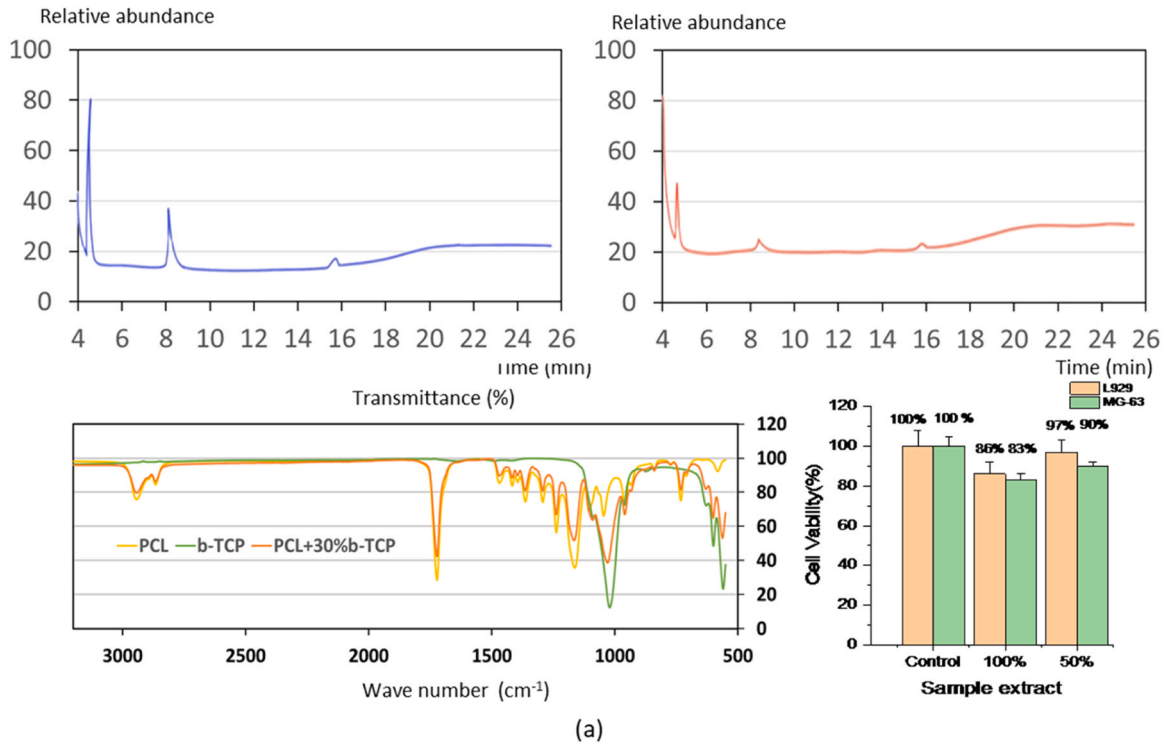

(a)

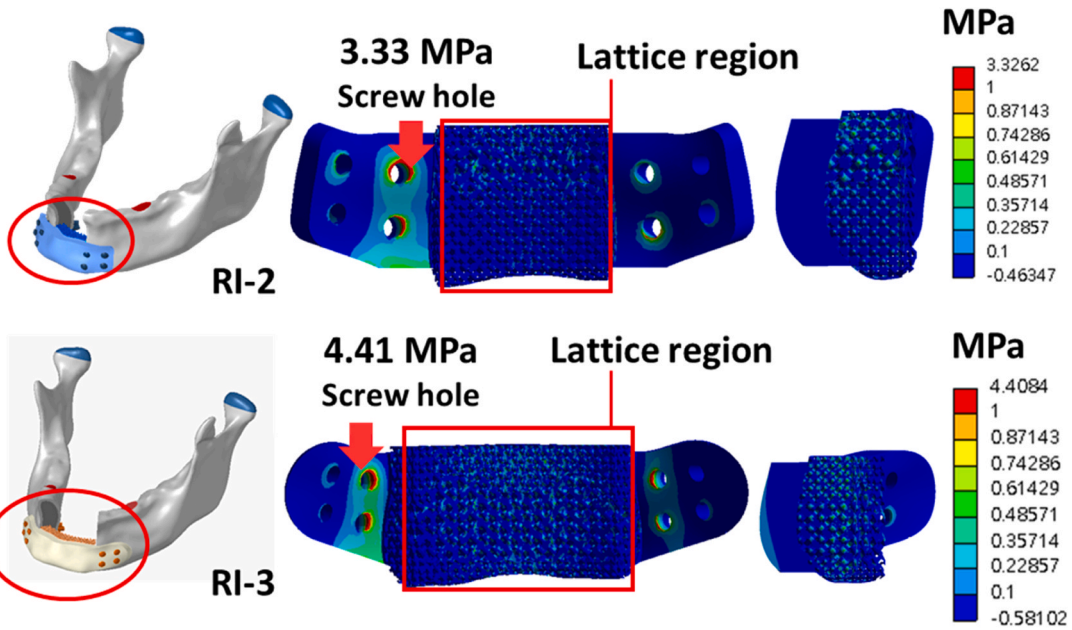

(b)

Fig. 8. (a) Top: GC-MS (Gas chromatography–mass spectrometry) analysis result. Bottom left: FTIR (Fourier-transform infrared spectroscopy) analysis result. Bottom right: MTT assay (tetrazolium-based cell viability test) result of L929 and MG63 cells; (b) Stress distribution maps of the reconstructed implants (RI-2 and RI-3) under loading conditions with different gradient lattice designs.

structure in the middle region showed relatively higher stress levels (yellow-green), indicating that this area may be subjected to greater bending moments. Compared to RI-2, the high-stress regions in the RI-3 model were broader and more dispersed, suggesting that RI-3 may be more prone to failure under the same loading conditions (Fig. 8(b)).

3.4. 3D printing accuracy

In this study, the use of 3D FDM printing technology enabled the gradient lattice pattern to be clearly visualized on the printed models (Fig. 5(a)). Table 3 lists the key dimensions of the three printed samples for RI-2 and RI-3 models, respectively, including TW, TH, LW, LH, HD and three different pores on three cross-sections (note section # - pore #) along with their corresponding measurements from reconstructed micro-CT images (shown in the left columns of the CT images in Figs. 5 (b) and 5(c)). The calculated results showed that all dimensional errors of the 3D FDM-printed PCL+ β-TCP materials were within 5 %.

3.5. Four-point bending test of reconstruction implant

In the static four-point bending test, corresponding values for the RI-2 and RI-3 models of average proof load were 83.75 ± 5.26 N and 35.73 ± 14.46 N (Fig. 6(b)), and bending strengths were 1465.63 ± 92.1 N-mm and 625.19 ± 252.98 N-mm, respectively. The proof load and bending strength of the RI-2 model were almost 2.35 times higher than those of the RI-3 model. The crack or failure patterns in the RI-2 and RI-3 groups were different. In the RI-2 model, only cracks were observed around the screw holes, and no fractures occurred in the side wings. In contrast, side wing fractures were found in the RI-3 model (Fig. 6(b)).

3.6. Standard degradation curve & hydrolytic degradation with dynamic loading test

The relationship between the percentage of mass loss in the lattice cube and actual time was found to be linear, as shown in Fig. 7(a). Therefore, mass loss can be converted to RI-2. Samples were subjected to dynamic loading at 1 Hz for 20,000 cycles. The 5.5-hour experiment approximately corresponds to 42.6 h of actual clinical effect (Table 4). The actual postoperative clinical period of one month is roughly equivalent to an experimental duration of 93 h.

Experimental results indicate that changes in PBS pH value were minimal and could be disregarded in both the RI-2 and RI-3 models (Table 4). In terms of weight loss, RI-2 samples exhibited an average decrease of approximately 6 %, while RI-3 samples decreased by about 8 %. Notably, none of the three RI-3 models withstood the simulated one-month period under the combined effects of water and loading, with damage occurring at around 14.4 days. Further observation revealed clear cracks and/or morphological defects around the screws securing the extended side wing and at the wing edges. In contrast, all three RI-2 models endured the one-month period under the same conditions without significant cracking or morphological damage (Fig. 7(c)).

Additional measurements of geometric changes in the three observation pores of each model (both RI-2 and RI-3) at three different sections (shown in the right columns of the CT images in Figs. 5(b) and 5(c) and statistical analysis from Tables 5 and 6) showed that, regardless of the model or section, geometric changes in the P08 lattice were consistently greater than those in the P06 lattice (upper of Fig. 7(c)). Across all models and sections, the average geometric change in Section 3 was greater than in Section 2, which was, in turn, greater than in Section 1. Overall, RI-3 showed significantly greater geometric changes compared to RI-2 (down of Fig. 7(c)). Further FE analysis of both models demonstrated that these results were proportional to sectional stress, indicating that higher stress corresponded to greater geometric changes (right part of Figs. 5(b) and 5(c)). In terms of macroscopic failure observation, all three RI-2 models showed no visible signs of damage after undergoing one month of simulated aqueous environment and dynamic loading (left of Fig. 7d). In contrast, representative RI-3 sample showing crack and fracture formation after 14.4 days of dual hydrolysis–loading (right-top of Fig. 7d). The right-middle of Fig. 7(d) illustrates the crack propagation path around the screw holes under optical magnification. The right-bottom of Fig. 7(d) presents the FE-predicted maximum principal stress vectors concentrated around the pore region, indicating a stress direction consistent with the observed crack path.

4. Discussion

The PCL + 30 % β-TCP composite material chosen for this study combines the flexibility of the plastic part with the bone-supporting properties of the ceramic part, providing both strength and biological activity. GC-MS analysis confirmed that ethyl acetate completely evaporated after the process, avoiding potential cytotoxicity; FTIR results also indicated that its composition was primarily a physical mixture, with no new chemical bonds formed, which helps maintain the predictable degradation behavior of the material. In addition, the MTT results show that the material is non-cytotoxic to L929 fibroblasts, and MG-63 osteoblast-like cells also maintained high viability (>80 %) under both extract concentrations, indicating good compatibility with both soft-tissue and bone-related cell types. Although the β-TCP content used here (30 wt%) is higher than the typical 10–20 % reported in previous studies [20], the composite still exhibited good processability and biocompatibility. The favorable MG-63 response further suggests that the high β-TCP fraction supports osteoblast activity and early bone-related integration, highlighting the material's potential as a high-strength, absorbable bone repair implant.

Compared to the low-stiffness bioprinting systems supported by hydrogel substrates [27], FDM technology can achieve higher resolution and print large, complex geometries, making it particularly suitable for load-bearing orthopedic implants that do not require immediate cell encapsulation. This study has overcome two major challenges in the development of absorbable ceramic composite implants at both the process and design levels, including material printability and microstructure controllability. First, although β-TCP is a common bone-conductive ceramic, its higher proportion usually effectively enhances the initial mechanical strength and bone mineralization potential of the composite material. However, in FDM printing, it causes significant processing bottlenecks: when the filler content exceeds 20 wt%, the viscosity and rheological properties of the molten mixture significantly increase, making it prone to nozzle clogging, unstable extrusion, or layer misalignment issues.

To address the challenges associated with incorporating high ceramic content into PCL, this study adopted prolonged ultrasonic dispersion and solvent evaporation to achieve a more uniform distribution of β-TCP within the polymer matrix, combined with optimized extrusion and printing temperatures. These processing strategies enabled the successful preparation and printing of stable filaments containing up to 30 wt% β-TCP without clogging or forming defects, thereby demonstrating the feasibility of fabricating high–ceramic content composites using FDM. The selection of 30 wt% β-TCP was further supported by previous systematic investigations of PCL/β-TCP composites. Bruyas et al. reported that formulations exceeding 40–60 wt% β-TCP exhibit particle agglomeration, increased brittleness, accelerated degradation, and even fabrication failure due to insufficient PCL to bind the ceramic phase [20]. Conversely, β-TCP contents below 20 wt% offer

Table 4
pH stability, weight loss, and their corresponding real-time degradation equivalents for RI-2 and RI-3 during dynamic loading.

	h degradation and dynamic loading		h degradation and dynamic loading.		RI-3 model after sample fractures	
	Average	Standard deviation	Average	Standard deviation	Average	Standard deviation
PH (Before)	7.40	0.00	7.40	0.00	7.40	0.00
PH (After)	7.44	0.03	7.41	0.08	7.40	0.07
Weight (mg) (Before)	3612.33	473.61	4124.00	96.06	4546.33	206.69
Weight (mg) (After)	3596.67	477.70	3868.00	114.59	4194.67	158.69
△Weight (mg)	15.67	4.51	256.00	28.21	351.67	132.32
△W (%)	0.45 %	0.17 %	6.00	16.00	8.00	23.00
Corresponding real time (hrs)	42.63	30.99	720.00 (one month)	0.00	345.64 (14.40 days)	114.21

Table 5
Comparison of the pore printing geometrical change errors at different cross- section between the printed and CAD-designed dimensions for the three RI-2 models before and after degradation.

	Pores at Section 1						**Pores at Section 2**						**Pores at Section 3**					
	Before degradation			After degradation			Before degradation			After degradation			Before degradation			After degradation		
Pore location (Fig. 5b)	1–1	1–2	1–3	1–1	1–2	1–3	2–1	2–2	2–3	2–1	2–2	2–3	3–1	3–2	3–3	3–1	3–2	3–3
Size in CAD-model	0.74	0.83	0.78				0.71	0.88	0.76				0.74	0.95	0.77			
Average measured size in CT image	0.74	0.85	0.77	0.88	1.07	0.87	0.67	0.87	0.77	0.81	1.13	0.93	0.71	0.93	0.76	0.89	1.23	0.96
Standard deviation	0.03	0.03	0.01	0.08	0.15	0.07	0.02	0.02	0.02	0.02	0.01	0.09	0.02	0.04	0.03	0.02	0.02	0.02
Error (%) between CAD & average CT image	0.00	2.41	-1.71				-2.90	-1.52	1.75				-3.60	-1.75	-1.30			
Error (%) of pore size before/after degradation (average)	19 (P06)	26 (P08)	13 (P06)	(13)			21 (P06)	30 (P08)	21 (P06)	(24)			25 (P07)	32 (P08)	26 (P06)	(28)		
Average error (%) of P06 vs P08 pores before/after degradation	16 [(19 +13)/ 2]	26					21 [(21 +21)/ 2]	30					25.5 [(25 +26)/ 2]	32				

P06/P08 = lattice types with different pore sizes.

Table 6
Comparison of the pore printing geometrical change errors at different cross- section between the printed and CAD-designed dimensions for the three RI-3 models before and after degradation.

	Pores at Section 1						**Pores at Section 2**						**Pores at Section 3**					
	Before degradation			After degradation			Before degradation			After degradation			Before degradation			After degradation		
Pore location (Fig. 5c)	1–1	1–2	1–3	1–1	1–2	1–3	2–1	2–2	2–3	2–1	2–2	2–3	3–1	3–2	3–3	3–1	3–2	3–3
Size in CAD-model	0.73	0.97	0.71				0.71	0.9	0.75				0.75	0.95	0.73			
Average measured size in CT image	0.72	0.97	0.73	0.98	1.44	0.84	0.72	0.94	0.74	1.01	1.45	0.95	0.74	0.95	0.72	1.32	1.45	0.90
Standard deviation	0.03	0.01	0.01	0.07	0.17	0.05	0.02	0.04	0.03	0.08	0.38	0.17	0.03	0.03	0.02	0.32	0.28	0.03
Error (%) between CAD & average CT image	-0.91	0.00	2.35				1.88	4.44	-0.89				-1.33	0.35	-1.83			
Error (%) of pore before/after degradation (average)	36 (P06)	33 (P08)	15 (P06)	(28)			40 (P06)	54 (P08)	28 (P06)	(41)			78 (P06)	49 (P08)	25 (P06)	(52)		
Average error (%) of P06 vs P08 pores before/after degradation	25.5 [(16 +15)/ 2]	33					34 [(40 +28)/ 2]	54					51.5 [(78 +25)/ 2]	59				

P06/P08 = lattice types with different pore sizes.

limited mechanical reinforcement and reduced osteoconductivity. Therefore, 30 wt% represents a practical and experimentally validated compromise that maintains filament integrity during FDM, provides adequate early-stage stiffness, and offers biologically favorable surface characteristics. This empirically supported ratio served as the optimal composition for the present study.

Secondly, this study also faces the engineering challenge of the inherent resolution limitations of the FDM system. Compared to photopolymerization or inkjet-based bioprinting technologies, FDM is limited by nozzle size and layer thickness control, making it unable to accurately reproduce fine pores smaller than 0.8 mm. If the lattice design is too small (e.g., pore size < 800 μm), it often becomes distorted or closed during physical printing due to material accumulation or layer edge blurring; conversely, if the pores are too large (> 2 mm), although it facilitates the penetration of liquids and nutrients, it can reduce cell adhesion efficiency, decrease support points, and even lead to early structural degradation and instability. This study selected the P06 lattice design (unit size: 2 mm, pillar 0.6 mm, pore size ~1000 μm, porosity 65 %), which has been verified to stably print clear and well-connected pore structures, while maintaining biologically suitable microenvironment parameters, providing good cell adhesion space and nutrient exchange channels. This design strategy achieves the optimal intersection between the "FDM printing limits" and "cell-friendly properties," providing significant insights for the future design of load-bearing regenerative implants.

After topological optimization and lattice configuration adjustment, the RI-2 design demonstrated significantly superior strength compared to RI-3 in the four-point bending test. FE analysis shows that under the same load, RI-3 exhibits a higher stress distribution, particularly concentrated around the wing plate and screw holes, which corresponds with the cracks and fracture patterns observed in the experiments. The reason RI-2 exhibits better endurance is that it withstands a smaller bending moment. In this study, the optimized structural design uses smaller units with higher density P06 lattices in high-stress areas, which can effectively reduce excessive stress concentration and provide a continuous supporting framework. This design not only enhances early postoperative stability but also reduces the risk of screw loosening and micromotion, which are key factors in determining whether the biodegradable implant can successfully support regeneration.

This study pioneers a dual simulation platform that combines hydrolytic environments with postoperative functional loading, successfully establishing a realistic physiological stress field faced by biodegradable implants in the early stages (one month after surgery) of critical mandibular defect reconstruction. The experimental design simulated the physiological fluid environment with 37°C PBS and applied dynamic compressive loads of 20–200 N at 1 Hz for up to 93 h, corresponding to the muscle traction load conditions in humans approximately one month after surgery. This is the first study to simultaneously investigate the dual effects of material degradation and structural fatigue on implant stability.

The results of dual simulations in PBS and dynamic load show that the RI-2 implant (with an arc length approximately twice the average width of the premolar–canine section) can maintain its complete structure and function within one month after surgery, with no significant deformation or damage observed. This confirms that its topologically optimized structure and lattice configuration provide sufficient support and degradation tolerance. This study controlled the size of the lattice units and the diameter of the pillars to create gradient P06 and P08 structures in areas with different stress levels, successfully balancing mechanical support and biological functions. In experiments simulating muscle traction and hydrolytic environments, the P06 region exhibited lower degradation and more stable deformation than those of P08. Additionally, the pore size of P06 is approximately 1000 μm with a porosity of 65 %, which theoretically facilitates rapid cell adhesion and growth. This means that in the most stressed parts of the implant, it needs to be strong enough after surgery to support bone growth, which greatly improves the chances of successful integration with the bone and the ability to properly repair the damaged area.

Moreover, the RI-3 implant—featuring an arc length approximately three times the width of the target section—exhibited pronounced fatigue cracks and structural collapse near the side wing screw hole after 14.4 days of dual testing under PBS immersion and dynamic loading. This suggests that its internal lattice configuration fails to effectively distribute stress, and the excessive span results in buckling and localized failure. In static failure testing, the structural tolerance of the RI-3 implant was markedly lower than that of RI-2, with its static bending strength reaching only 43 % of RI-2's. Taken together, these results indicate that the failure risk of the RI-3 implant may be three to four times greater than that of RI-2, underscoring the importance of proper topological design and stress dispersion in ensuring implant durability and mechanical stability.

Under simulated experimental conditions, hydrolysis gradually weakens both the material's cross-sectional integrity and molecular structure. However, the primary driver of substantial structural damage is the localized stress concentration and crack propagation induced by continuous dynamic loading. These two mechanisms—hydrolytic degradation and fatigue loading—act synergistically, but fatigue loading serves as the principal trigger for failure initiation. Compared to RI-2, the RI-3 implant experiences a higher bending moment, resulting in elevated stress levels and an accelerated rate of hydrolysis, particularly in high-stress regions such as the mid-span section (Fig. 8(b)). These findings demonstrate that when employing 3D-printed biodegradable implants for reconstruction in load-bearing regions, the ratio of the reconstructed arc length (AL) to the combined width of the residual bone stumps ($WR + WL$) should be maintained below 2.0. This constraint helps ensure a reasonable stress distribution and structural stability during the early postoperative period.

By combining topological optimization with gradient lattice designs, we can set a minimum level of mechanical support and a safe range for shapes that are important for successful healing in the early stages. In the future, this combined simulation approach and the related geometric ratio standards could help create a "structural regeneration threshold," which would be a new way to design and assess biodegradable load-bearing implants, offering clear guidelines for their use in regenerative medicine.

Although this study has established a comprehensive workflow encompassing material preparation, structural design, mechanical simulation, and preliminary dynamic validation, several limitations should be acknowledged and addressed in future work. First, the current experimental platform is limited to in vitro conditions, lacking the biological complexity of bone cell migration, tissue growth, and angiogenesis. Future studies should incorporate in vivo animal models to assess true osseointegration and the degradation behavior of the implants. Second, the present analysis focuses solely on a representative case of a large anterior mandibular defect, without validating the approach across the diverse clinical presentations of bone defects. Broader anatomical and pathological variations should be considered to enhance clinical applicability.

Moreover, the implant design intentionally preserves spatial and structural features to accommodate auxiliary functional modules, such as surface coatings with growth factors or antibacterial agents, internal cavity filling with platelet-rich fibrin (PRF) or synthetic bone grafts to promote faster bone bridging, and incorporation of drug reservoirs (e.g., platinum-based hydrogels) for localized therapy, especially in post-tumor resection scenarios. This modular and adaptable design platform exemplifies the interdisciplinary integration of clinical needs with biomedical engineering. It holds strong potential to drive the next generation of bone implants characterized by multifunctionality, personalization, and time-controlled therapeutic capabilities.

5. Conclusion

This study successfully demonstrated a comprehensive workflow for the development of biodegradable, 3D-printed, topology-optimized mandibular reconstruction implants, integrating material synthesis, lattice structure design, mechanical evaluation, and dual-mode degradation simulation. The RI-2 design, characterized by a shorter arc length and high-density P06 lattice in critical stress zones, exhibited superior mechanical strength, dimensional stability, and resistance to hydrolytic degradation compared to the RI-3 design. The dual simulation platform—incorporating physiological hydrolysis and cyclic loading—realistically replicated early postoperative conditions and revealed critical design thresholds for implant stability. These findings suggest that maintaining the reconstruction arc length within twice the width of the residual bone and employing stress-adaptive lattice configurations are essential for achieving early-stage mechanical support and guiding bone regeneration. This study not only provides valuable insights into the structural and biological optimization of load-bearing biodegradable implants but also lays the groundwork for establishing quantitative design criteria for further clinical application.

CRediT Authorship contribution statement

Hsuan-Wen Wang: Writing – original draft, Investigation, Data curation. Chiao-Min Chang: Writing – original draft, Methodology, Data curation. Wei-Che Tsai: Investigation, Data curation. Yen Cheng: Investigation, Data curation. Pao-Wei Lee: Data curation. Chun-Li Lin: Writing – review & editing, Supervision, Funding acquisition, Conceptualization.

Declaration of Competing Interest

The authors, Hsuan-Wen Wang, Chiao-Min Chang, Wei-Che Tsai, Yen Cheng, Pao-Wei Lee, Chun-Li Lin declare that we have no proprietary, financial, professional or other personal interest of any nature or kind in any product, service and/or company that could be constructed as influencing the position presented in, or the review of, the manuscript entitled, “Early-stage stability and degradation of patient-specific biodegradable 3D-printed implants for critical mandibular reconstruction”. The authors declare that they have no known competing financial interests or personal relationships that could have appeared to influence the work reported in this paper.

Acknowledgements

This study is supported in part by NSTC project 108–2622-E-010–001 -CC2, 110–2222-E-032–003 -MY2 and 113–2327-B-A49 −001, Taiwan.

References

[1] Shu Z, Li H, Gao L. An efficient data-driven optimization framework for elastically isotropic lattice structures. Mater Des 2025;253.
[2] Kumar BP, Venkatesh V, Kumar KA, Yadav B, Ram Mohan S. Mandibular reconstruction: overview. J Maxillofac Oral Surg 2016;15:425–41. https://doi.org/10.1007/s12663-015-0766-5.
[3] Lee SW, Kim HG, Ham MJ, Hong DGK, Kim SG, Rotaru H. Custom implant for reconstruction of mandibular continuity defect. J Oral Maxillofac Surg 2018;76:1370–6. https://doi.org/10.1016/j.joms.2017.12.003.
[4] Patel A, Harrison P, Cheng A, Bray B, Bell RB. Fibular reconstruction of the maxilla and mandible with immediate implant-supported prosthetic rehabilitation: jaw in a day. Oral Maxillofac Surg Clin North Am 2019;31:369–86. https://doi.org/10.1016/j.coms.2019.03.002.
[5] Toure G, Gouet E. Use of a 3-dimensional custom-made porous titanium prosthesis for mandibular body reconstruction with prosthetic dental rehabilitation and lipofilling. J Oral Maxillofac Surg 2019;77:1305–13. https://doi.org/10.1016/j.joms.2018.12.026.
[6] Lin CL, Wang YT, Chang CM, Wu CH, Tsai WH. Design criteria for patient-specific mandibular continuity defect reconstructed implant with lightweight structure using weighted topology optimization and validated with biomechanical fatigue testing. Int J Bioprint 2022;8:437. https://doi.org/10.18063/ijb.v8i1.437.
[7] Li CH, Wu CH, Lin CL. Design of a patient-specific mandible reconstruction implant with dental prosthesis for metal 3D printing using integrated weighted topology optimization and finite element analysis. J Mech Behav Biomed Mater 2020;105:103700. https://doi.org/10.1016/j.jmbbm.2019.103700.
[8] Rana M, Buchbinder D, Sánchez, Aniceto G, Mast G. Patient-specific solutions for cranial, midface, and mandible reconstruction following ablative surgery: expert opinion and a consensus on the guidelines and workflow. Craniomaxillofac Trauma Reconstr 2025;18:15. https://doi.org/10.3390/cmtr18010015.
[9] Kreutzer K, Steffen C, Koerdt S, Doll C, Ebker T, Nahles S, Flügge T, Heiland M, Beck-Broichsitter B, Rendenbach C. Patient-specific 3D-printed miniplates for free flap fixation at the mandible: a feasibility study. Front Surg 2022;9:778371. https://doi.org/10.3389/fsurg.2022.778371.
[10] Almudarris BA, Rajput T, Singh V, Feroz Abdul, Qurishi SM, Homeida AA. JHE. Outcomes of using 3D-printed titanium implants in mandibular reconstruction. J Pharm Bioallied Sci 2025;17(2):S1529–31. https://doi.org/10.4103/jpbs.jpbs_1816_24.
[11] Popat SP, Gupta A, Khismatrao VN, Batra H, Meena VK. Management of failed patient-specific implant used for mandibular reconstruction: a case report. J Maxillofac Oral Surg 2023. https://doi.org/10.1007/s12663-023-02054-8.
[12] Subash P., Nerurkar S.A., Krishnadas A., Vinay V., Iyer S., Manju V. Patient-specific alloplastic implant reconstruction of mandibular defects–safe practice recommendations and guidelines. J Maxillofac Oral Surg. 2323; 22 Suppl 1: 28–36. https://doi.org/10.1007/s12663-023-01881-z.
[13] Maintz M, Tourbier C, de Wild M, Cattin PC, Beyer M, Seiler D, Honigmann P, Sharma N, Thieringer FM. Patient-specific implants made of 3D printed bioresorbable polymers at the point-of-care: material, technology, and scope of surgical application. 3D Print Med 2024;10:13.
[14] Kallivokas SV, Kontaxis LC, Psarras S, Roumpi M, Ntousi O, Kakkos I, Deligianni D, Matsopoulos GK, Fotiadis DI, Kostopoulos V. A combined computational and experimental analysis of PLA and PCL hybrid nanocomposites 3D printed scaffolds for bone regeneration. Biomedicines 2024;12:261.
[15] Fairag R, Li L, Ramirez-GarciaLuna JL, Taylor MS, Gaerke B, Weber MH, Rosenzweig DH, Haglund L. A composite lactide-mineral 3D-printed scaffold for bone repair and regeneration. Front Cell Dev Biol 2021;9:654518.
[16] Ghezzi B, Matera B, Meglioli M, Rossi F, Duraccio D, Faga MG, Zappettini A, Macaluso GM, Lumetti S. Composite PCL scaffold with 70% β-TCP as suitable structure for bone replacement. Int Dent J 2024;74:1220–32.
[17] Liu HC, Chan YH, Huang SF, Tsai WC, Cheng Y, Lin CL. Early stage prediction of bone regeneration using FEA and cell differentiation algorithms with 3D-printed PLA and PCL scaffolds: modeling and application to dorsal double plating in distal radius fractures. 3D Print Med 2025;11:30. https://doi.org/10.1186/s41205-025-00278-7.
[18] Eichholz KF, Freeman FE, Pitacco P, Nulty J, Ahern D, Burdis R, Browe DC, Garcia O, Hoey DA, Kelly DJ. Scaffold microarchitecture regulates angiogenesis and the regeneration of large bone defects. BioFabr 2022;14(4). https://doi.org/10.1088/1758-5090/ac88a1.
[19] Barkow P, Polley C, Schöbel L, Schnell G, Springer A, Bader R, Boccaccini AR, Seitz H. 3D printing of microstructured piezoelectric and bioactive PCL-composite scaffolds for bone regeneration. Int J Bioprint 2025;11:216–33. https://doi.org/10.36922/ijb.5964.
[20] Bruyas A, Lou F, Stahl AM, Gardner M, Maloney W, Goodman S, Yang YP. Systematic characterization of 3D-printed PCL/β-TCP scaffolds for biomedical devices and bone tissue engineering: influence of composition and porosity. J Mater Res 2018;33:1948–59. https://doi.org/10.1557/jmr.2018.112.
[21] Gharibshahian M, Salehi M, Beheshtizadeh N, Kamalabadi-Farahani M, Atashi A, Nourbakhsh M, Alizadeh M. Recent advances on 3D-printed PCL-based composite scaffolds for bone tissue engineering. Front Bioeng Biotechnol 2023;11:1168504. https://doi.org/10.3389/fbioe.2023.1168504.
[22] Başöz D, Karaman Mİ, Büyüksungur S, Yucel D, Hasırcı N, Kocaoglu B, Hasirci V. 3D printed PCL-nHAp composite implants for the treatment of segmental bone defects: in vivo application in a rabbit model. BioFabr 2024. https://doi.org/10.1088/1758-5090/ad9fe1.
[23] ISO 10993-5. Biological evaluation of medical devices – Part 5: Tests for in vitro cytotoxicity. Geneva: International Organization for Standardization; 2009.
[24] ASTM D638, Standard test method for tensile properties of plastics.
[25] Lai PL, Chang CM, Huang SF, Liu PH, Lin CL. Designing an anatomical contour titanium 3D-printed oblique lumbar interbody fusion cage with porous structure and embedded fixation screws for patients with osteoporosis. Int J Bioprint 2023;9:445–58.
[26] Wu CH, Wu HK, Tsai PJ, Lin CL. Early monitoring for 3D-printed patient-specific mandible reconstructive implant biomechanical behavior under different occlusal conditions using a wireless module system. Int J Bioprint 2024;10(3):2553. https://doi.org/10.36922/ijb.2553W.
[27] Schupp, Arzdorf M, Linke B, Gutwald R. Biomechanical testing of different osteosynthesis systems for segmental resection of the mandible. J Oral Maxillofac Surg 2007;65:924–30. https://doi.org/10.1016/j.joms.2006.06.30.